

# Triggered slip on a back reverse fault in the Mw6.8 2013 Lushan, China earthquake revealed by joint inversion of local strong motion accelerograms and geodetic measurements



Guohong Zhang<sup>a,b,\*</sup>, Eric A. Hetland<sup>b</sup>, Xinjian Shan<sup>a</sup>, Martin Vallée<sup>c</sup>, Yunhua Liu<sup>a</sup>, Yingfeng Zhang<sup>a</sup>, Chunyan Qu<sup>a</sup>

<sup>a</sup> State Key Laboratory of Earthquake Dynamics, Institute of Geology, China Earthquake Administration, Beijing 100029, China

<sup>b</sup> Earth and Environmental Sciences, University of Michigan, Ann Arbor, USA

<sup>c</sup> Institut de Physique du Globe de Paris, Sorbonne Paris Cité, Université Paris Diderot, UMR 7154 CNRS, Paris, France

## ARTICLE INFO

### Article history:

Received 4 June 2015

Received in revised form 11 January 2016

Accepted 13 January 2016

Available online 6 February 2016

### Keywords:

Triggered fault slip

Back reverse fault

Joint inversion

Local strong motion data

Geodetic measurements

The 2013 Lushan earthquake

## ABSTRACT

The 2013 Mw6.8 Lushan, China earthquake occurred in the southwestern end of the Longmenshan fault zone. We jointly invert local strong motion data and geodetic measurements of coseismic surface deformation, including GPS and InSAR, to obtain a robust model of the rupture process of the 2013 Lushan earthquake. Our joint inversion best model involves the rupture of two opposing faults during the Lushan earthquake, a main fault and a secondary fault. It is only when the secondary fault is included that both the GPS and InSAR measurements are fit along with the near-field strong motion. Over 75% of the computed moment was released in slip on the main fault segment, a northwest dipping, listric thrust fault, with buried thrust and dextral strike-slip at hypocenter depths, and with only minor slip closer to the surface. The secondary fault mainly involved oblique thrust slip or pure dextral strike-slip at shallower depths, and accounts for just under 24% of the moment released in the Lushan earthquake. Coulomb stress changes of about 0.5 MPa on the secondary fault segment at the time coseismic slip initiated on that fault indicate that slip was likely triggered by the coseismic slip on the main blind thrust fault. Our coseismic slip model is consistent with a sub-horizontal and east–west to southeast–northwest trending most compressive stress. Our inferred coseismic slip model is also consistent with previous GPS derived models of strain accumulation on the Longmenshan fault system.

© 2016 Elsevier B.V. All rights reserved.

## 1. Introduction

The magnitude 6.8 Lushan earthquake occurred on April 20, 2013 in Sichuan province, China, and resulted in 198 casualties, tens of thousands of injuries, and damages totaling 6.8 billion USD (EM-DAT). The epicenter of the Lushan earthquake is located at (30.291°N, 102.983°E) and the hypocentral depth is 17.6 km (Fang et al., 2013). The Lushan region is in the southwestern part of the Longmenshan fault zone (LMSF), which also hosted the 2008 Mw7.9 Wenchuan earthquake to the northeast. The LMSF is the margin between the Tibetan plateau and the Sichuan Basin, and is a northeast–southwest striking and northwest dipping fault zone (Burchfiel, 2008; Fig. 1a). The LMSF had been widely considered to be of low earthquake risk before the 2008 Wenchuan earthquake, due to the low level of seismicity on the LMSF and the slow moment accumulation rate inferred from geodetic observations (Zhang, 2013), although including non-elastic effects in the earthquake cycle model may reconcile the low GPS rates with a short recurrence time of large earthquakes (Thompson et al., 2015).

The Lushan earthquake occurred roughly 90 km to the southwest of the 2008 Wenchuan earthquake (Fig. 1). Parsons et al. (2008) inferred only a slight positive coulomb stress change (CSC) contribution from the Wenchuan earthquake in the region of the Lushan earthquake. To date, there have been no other significant earthquakes on the LMSF (Zhang et al., 2010), and the region between the Lushan and Wenchuan earthquakes likely poses a significant ongoing earthquake risk (e.g., Shan et al., 2013).

The Lushan earthquake occurred in a complex tectonic region, just to the north of an area that can be loosely referred to as a triple junction, with the Sichuan Basin to the east and the Songpan and Dianzhong blocks to the northwest and south, respectively (Fig. 1a). The LMSF is the boundary between the Songpan block and the Sichuan Basin, and the Songpan block is bounded by the Xianshuihe fault (XSHF) on the west. To the south, the Anninghe fault (ANHF) separates the Dianzhong block from the Sichuan Basin (Fig. 1). Both the XSHF and ANHF are large active strike-slip faults, with a dextral strike-slip rate of > 10 mm/yr and 3–8 mm/yr, respectively (e.g., King et al., 1997; Wang et al., 2008). In contrast, the LMSF has components of both thrust and dextral strike-slip motion, which was revealed by GPS observations prior to the 2008 Wenchuan earthquake (e.g., Shen et al., 2005; Meade, 2007), as

\* Corresponding author at: Hua Yan Li Jia Yi Hao, Chaoyang district, Beijing 100029, China.  
E-mail address: zhanggh@ies.ac.cn (G. Zhang).

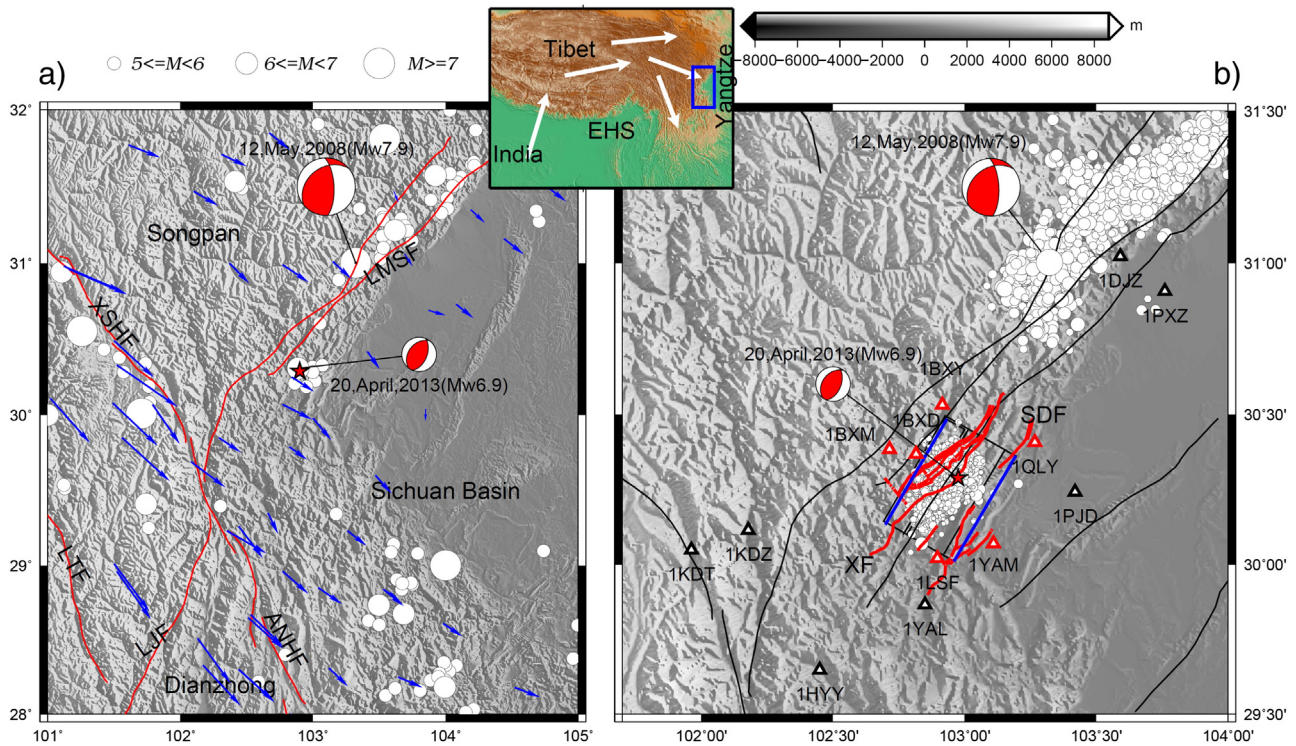


**Fig. 1.** Tectonic setting of the 2013 Lushan earthquake, with locations of the strong motion stations (red triangles), mapped faults (solid lines), epicenters of earthquakes  $M_s > 5.0$  between 1901 and 2014 from Global CMT (which circles, symbol size scales with magnitude), and epicenter of the 2013 Lushan earthquake (red star). (a) The two focal mechanisms are the 2008 Wenchuan and the 2013 Lushan earthquakes. GPS measured crustal motion by Gan et al. (2007) is shown as blue vectors. (b) Thick red lines and triangles are local faults and stations, respectively. Triangles with thick red outlines are stations displayed in Fig. 4, which are used to demonstrate the differences between the optimal inversion and the inversion test without it. Black outlines are stations not used for comparison between the optimal inversion and the inversion test. Blue lines are intersections of the fault model projected to the surface. Acronyms: EHS, Eastern Himalaya Syntaxis; YZ, Yangtze; XSHF, Xianshuihe fault; LMSF, Longmenshan fault; LJJF, Lijiang–Xiaojinhe fault; ANHF, Anninghe fault; XF, (Zemuhe–)Xiaojiang fault; LTF, Litang fault; XF: Xinkaidian fault; SDF: Shuangshi–Dachuan fault. (For interpretation of the references to color in this figure legend, the reader is referred to the online version of this chapter.)

well as coseismic slip models of that earthquake (e.g., Medina Luna and Hetland, 2013; Styron and Hetland, 2015).

Field investigations conducted after the Lushan earthquake, focal mechanisms of the earthquake, and distribution of aftershocks all suggest that there is a degree of complexity in the geometry of the faults that ruptured in the Lushan earthquake (Li et al., 2013; Xu et al., 2013; Fang et al., 2013). Li et al. (2013) argued that the local geologic setting of the 2013 Lushan region is very complicated, consisting of both northeast striking faults, consistent with the overall trend of the LMSF, and northwest striking transform faults. They also pointed out that the Lushan event initiated on a detachment underneath the frontal Longmenshan range between the Shuangshi–Dachuan fault (SDF) and the Xinkaidian fault (XF) based on observations of surface cracks indicative of slip on a shallow dipping fault at depth (Li et al., 2013). Li et al. (2014) further argued that the Lushan earthquake occurred on a portion of a blind thrust at the front of the Longmenshan range, which is linked to a detachment that extends into the Sichuan basin. Focal mechanisms determined for the Lushan earthquake by Global CMT and USGS W-phase CMT indicated that the coseismic slip was thrust; however, several of the focal mechanisms contained non-double-couple components, which might either be due to poor resolution of the inferred focal mechanism or may also indicate a variation in fault geometry or rake in the Lushan earthquake. Finally, relocated aftershocks reveal a cluster of events extending into the hanging wall of the thrust fault that likely ruptured in the Lushan earthquake (Fang et al., 2013; Fig. 2a). The larger Wenchuan earthquake that occurred to the northeast on the LMSF was characterized by fairly complicated coseismic slip, with large rake variations on variably dipping faults (e.g., Shen et al., 2009; Feng et al., 2010; Zhang et al., 2011; Wang et al., 2011). Given the complexity of slip in the earlier Wenchuan earthquake, it might

follow that the Lushan earthquake might also be characterized by complexities in slip, albeit to a lesser degree and with more compact slip than in the Wenchuan earthquake, due to the fact that the 2013 Lushan event has much smaller magnitude. Additionally, since the 2008 Wenchuan event obliquely ruptured an unusually highly dipping ( $\sim 50^\circ$  in the shallow portions of the fault), listric fault (Zhang et al., 2010), it is natural to ask whether the Lushan event also involved slip on a low-angle detachment at depth or if it was entirely constrained on a high-angle thrust fault.

There have been several published coseismic slip models of the Lushan earthquake. Hao et al. (2013) and Zhang et al. (2014) both used local strong motion and teleseismic data and inferred similar slip distribution models, demonstrating predominantly thrust motion on a relatively high-angle blind fault. Jiang et al. (2014) derived a fault slip model based on local GPS data, and indicated that the GPS data required significant sinistral strike-slip in addition to the dominant thrust slip. Note that these previous studies all assumed single, planar fault geometries, and used either the seismic or geodetic data separately. As the regional tectonic setting is somewhat complex, the assumption that only a single planar fault slipped in the Lushan earthquake may not be complete. Moreover, using both seismic and geodetic data it may be possible to better constrain the fault geometry and rupture process (see Supplementary material).

In this study, we infer the fault geometry and spatio-temporal evolution of the rupture process in the 2013 Lushan earthquake using a joint inversion of local strong motion, GPS, and InSAR data. The strong motion stations we use are all relatively close to the source area (Fig. 1b), and the data from them provides valuable constraints on the spatiotemporal coseismic slip distribution (see Supplementary material), allowing us to determine whether there are some delayed or triggered slip in the

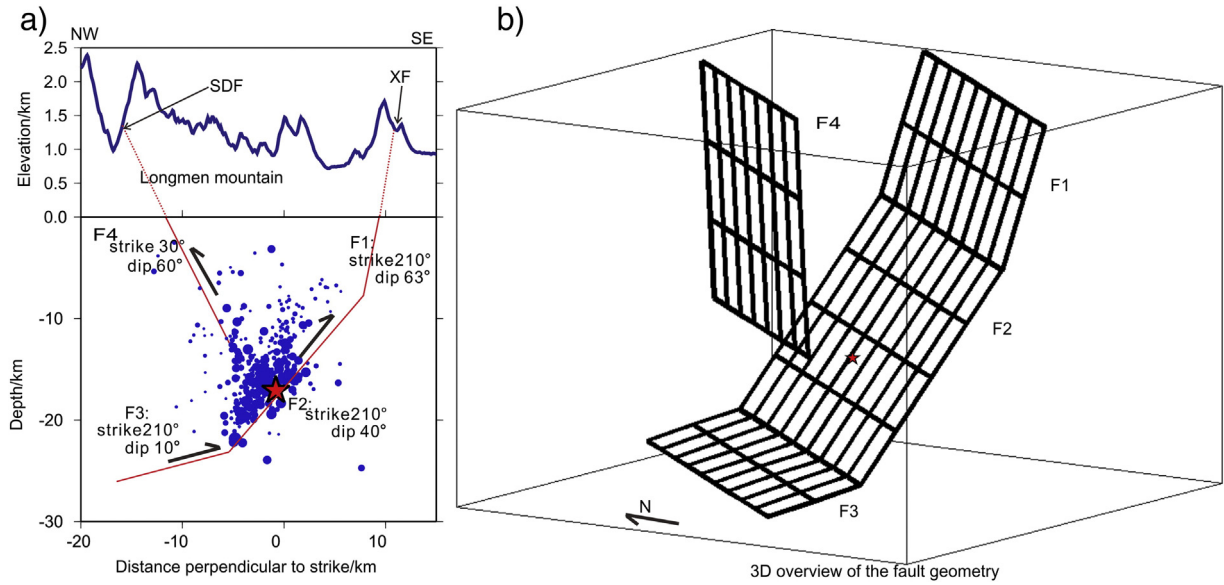


**Fig. 2.** The preferred fault model used in the joint inversion. (a) Aftershocks and fault dip variation along a cross section perpendicular to the trend of the Lushan fault. (b) 3D overview of the fault model.

Lushan earthquake, as was detected for the Wenchuan earthquake (Zhang et al., 2012). GPS and InSAR measurements provide independent constraints on the static final slip distribution (see Supplementary material). We follow the same inversion strategy of Delouis et al. (2002). We use the geodetic data as the primary constraint on the fault geometries and we use the strong motion data to infer the spatiotemporal coseismic slip, with the constraint that the total coseismic slip fits the geodetic data. Below we describe the data, the methodology of rupture inversion, and the inference of the fault geometry model, and then discuss the inferred spatiotemporal coseismic slip.

## 2. Data

### 2.1. Strong motion data

The local strong motion accelerograms are provided by the National Strong-Motion Observation Network System (NSMONS) of China. We use 38 components recorded by 13 stations (Fig. 1b), out of the 276 components available in the entire network. We choose the components according to the signal-to-noise (SNR) level of each record, as well as the distance to the epicenter and the azimuthal coverage. All of the selected stations are located within ~100 km from the epicenter and are relatively uniformly distributed around it. The closest station is 5.8 km away from the epicenter and the farthest is 97.6 km. We bandpass the strong motion record using a low-pass frequency cutoff of 0.3 Hz because higher frequency modeling would require a better knowledge of the crustal structure. We determine the high-pass frequency cutoff for each component separately, based upon the SNR of the record. Depending on the data quality, this cutoff varies between 0.012 Hz and 0.031 Hz. The accelerograms were then integrated twice to get the ground displacements.

### 2.2. Geodetic data

We use RadarSAT-2 SLC data (which is C band with a wavelength of ~5.6 cm) to obtain the coseismic deformation of the Lushan earthquake along the satellite line-of-sight (LOS; Fig. 3a). Full details of the InSAR processing are given in the Supplementary material, and we compute two coseismic interferograms of duration 120 and 312 days (Table S2). The interferograms only resolve coseismic displacements to the east of the Lushan epicenter, primarily in the Sichuan Basin and on the footwall of

the thrust fault. There are large LOS signals far from the fault, at distances where an earthquake of this magnitude would not produce coseismic ground displacement (Fig. S2). These artifacts are likely caused by nonlinear factors such as atmospheric turbulence. We use GPS measurements of coseismic displacements from Jjang et al. (2014), which reveal relative thrusting motion between the LMSF zone and the Sichuan basin (Fig. 3a). Despite being sparsely distributed, the GPS measurements provide another independent constraint on the coseismic slip (see Supplementary material). The InSAR measured displacements qualitatively agree well with the GPS measurements (see Supplementary material).

## 3. Methodology of rupture inversion

We use a similar inversion scheme as we used to study the Wenchuan earthquake (Zhang et al., 2012), which is based on Delouis et al. (2002). In this method, the source fault is represented by a discontinuity in an elastic half-space and is discretized along the fault strike and dip in  $5 \times 5$  km<sup>2</sup> patches, referred to as “sub-faults” here. A multi-time window method is used to simulate the source time function (STF) of each sub-fault, which is represented by three, mutually overlapping isosceles triangular functions with 1 s half-duration (Olson and Aspel, 1982). Such an inversion scheme allows a sub-fault to slip more than once and also allows locally delayed rupture (Zhang et al., 2012). The onset time of each sub-fault relative to the earthquake initiation is determined using an average rupture velocity, and we consider a large variation from 1.0 to 3.8 km/s. The rake boundary is set to  $90^\circ \pm 20^\circ$ , to be consistent with the focal mechanism of the Lushan event. We use a simulated annealing scheme to solve the non-linear inversion, minimizing both the weighted normalized root mean square (WNRMS) misfit of all the data sets and mismatch of the computed moment with an a-priori moment (Delouis et al., 2002). Details on how the simulated annealing method works can be found in a previous study (Fig. 5 in Zhang et al., 2013). The cost function that we use is

$$F_{cost} = WNRMS + \exp(M_{0-cal}/M_0 - 1) \cdot C_{\min M_0}$$

$$WNRMS = \frac{W_{SM} \cdot NRMS_{SM} + W_{INSAR} \cdot NRMS_{INSAR} + W_{GPS} \cdot NRMS_{GPS}}{W_{SM} + W_{INSAR} + W_{GPS}}$$

where  $F_{cost}$  is the total cost function,  $NRMS_X$  is the normalized root mean square difference between the model prediction and data X, and  $W_X$  is a weight assigned to data X.  $M_{0-cal}$  and  $M_0$  are the computed seismic

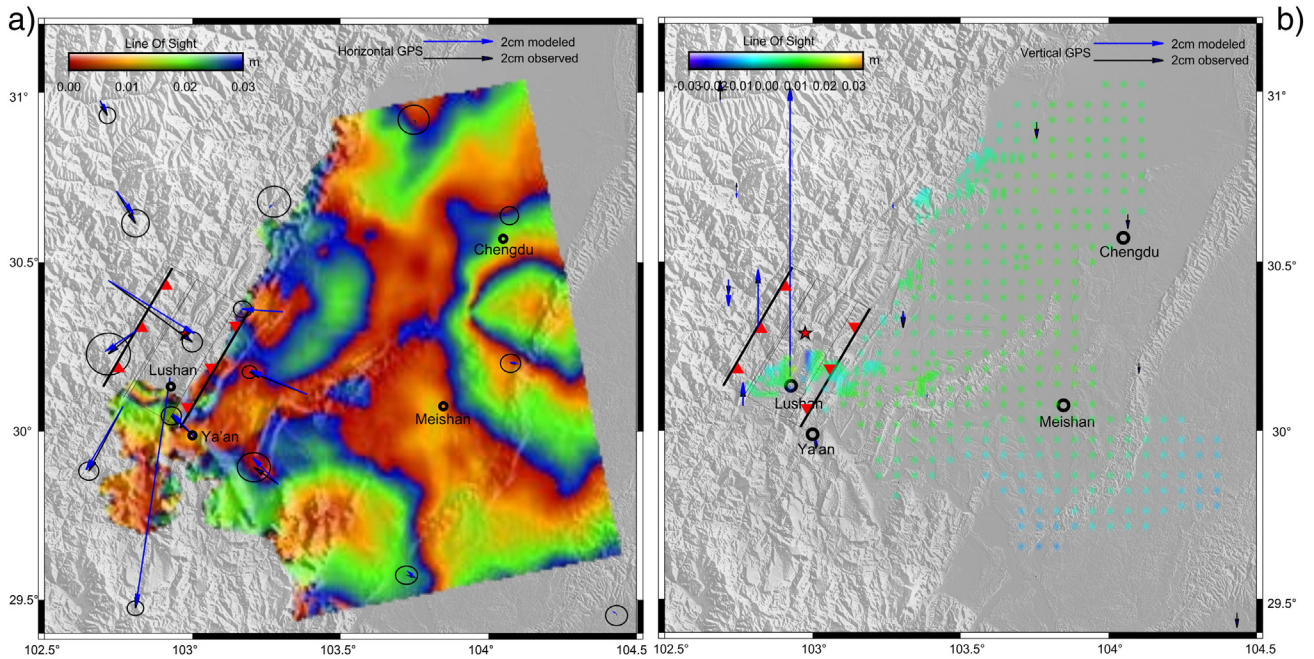


**Fig. 3.** Coseismic deformation detected by GPS and InSAR. (a) A color cycle from red to blue equals 3 cm surface deformation in the line-of-sight direction (LOS), obtained by InSAR. Black and blue arrows are horizontal GPS observations with 90% of confidence ellipses and predictions by joint inversion, respectively. Black straight lines are the surface projections of our preferred fault model. (b) Color dots showing the residuals of the InSAR data used during joint inversion. Black and blue arrows are vertical GPS observations and predictions by joint inversion, respectively. (For interpretation of the references to color in this figure legend, the reader is referred to the online version of this chapter.)

moment from our inversion and the moment from Global Centroid Moment Tensor inversion, respectively. The minimization of moment is included due to the fact that the inverted seismic moment is usually found to be over-estimated (Delouis et al., 2002).  $C_{\min M_0}$  weights the minimization of the moment in the total cost, and we use 0.1, which we determine by several preliminary inversion tests. From these preliminary tests, we also choose the weight of each data set to be equal. We note variations of the minimization constraint of the computed moment and data weight would change the inverted slip distribution within a certain level; however, we find that varying the weights does not significantly change the main features of our preferred Lushan slip model, and for simplicity we equally weight the seismic, GPS, and InSAR data.

An earth velocity model is needed for computing theoretic seismograms. Lateral heterogeneity between eastern Tibet and the Sichuan basin may be an important factor during the near-field seismogram modeling. In our previous study we determined a layered velocity model for modeling the Wenchuan mainshock strong motion waveforms through analyzing its two aftershocks. The simplified velocity model is appropriate for modeling the relatively low frequency cutoff of 0.1 Hz (Zhang et al., 2012). In the current Lushan study, we used a high frequency cutoff of 0.3 Hz. Thus we improved the velocity model according to a high resolution earth model by Liu et al. (2014). The updated velocity model includes possible lateral crustal heterogeneity within the source region, and has not only a low velocity sedimentary lid layer for stations in Sichuan Basin, but also a low velocity layer at mid-crust depth for stations within eastern Tibet (see Supplementary material). Based on these high resolution velocity model and the analytical expressions by Johnson (1974), we simulate synthetic near-field accelerogram on each strong motion station produced by simple shear dislocation (double-couple) point sources. In addition, we calculate the Green's function of GPS and InSAR under a uniform, isotropic elastic half-space using the dislocation formulation of Savage (1980).

#### 4. Fault model

Due to the fact that coseismic slip in the Lushan earthquake did not reach the surface (Xu et al., 2013; Li et al., 2013), determining an initial

fault model is not straightforward, and we followed multiple steps to converge to the final fault model. Due to the proximity of the epicenter to the XF and the SDF (Fig. 1b), it is possible that the Lushan earthquake involved rupture on either of these two faults. As these faults are mapped, slip in previous earthquakes on these faults must have reached the surface, although there was no surface rupture associated with the Lushan earthquake (Xu et al., 2013). We estimate the strike and length of the main fault segment using relocated aftershocks from Fang et al. (2013); Fig. 2a. We set the strike to be  $210^\circ$  (i.e., roughly SW–NE striking) and a length of 45 km long along strike. This strike is consistent with the focal mechanisms and the InSAR data, although we note that with no surface rupture that would have resulted in discontinuities in the InSAR fringes, we cannot exactly map the fault from the InSAR data. Due to the scatter in the aftershocks, we do not estimate the fault dip from the aftershock hypocenters. Unlike previously published studies that assume a single planar fault model, we allow for a listric fault geometry (i.e., steep at shallow depths, and low-angle at depth), by assuming that the fault is composed of up to four 10 km wide segments. We do not allow the dip to vary along strike. We assume that the dip of each of the fault segments changes linearly with depth, and adjacent segments are allowed to have constant dip, so a single planar fault segment would be permissible. We then iterate over dips of the deepest and shallowest segments, assuming that the dip of the deepest fault segment is less than the shallowest segment, and that the fault passes through the hypocenter of the Lushan earthquake. The dip angles of the shallowest segment and the deepest segment were initially set to be  $1^\circ$  and  $70^\circ$ , respectively and grid searched by a step of  $1^\circ$ . For each of the candidate fault dips, we invert the GPS and InSAR measurements assuming uniform slip on the planar fault segments. We do not use the strong motion data during this initial inversion, since the assumption of uniform slip on 45 km long and 10 km wide planar fault segments is a too gross assumption to adequately describe the strong motion records. However, the purpose of this initial inversion is to only constrain the fault geometry.

We find that the geodetic data are well described using a fault model with three fault segments (Fig. 2a). The shallowest segment, F1, is 10 km wide and dipping  $63^\circ$ , the middle segment, F2, is 20 km wide and

dipping 40°, and the deepest segment is 10 km wide and dipping 10°. We refer to segments F1–F3 collectively as “the main fault” hereinafter. The surface trace of F1 corresponds to the mapped trace of XF (Fig. 1b), indicating that the Lushan earthquake involved slip on that fault.

Field surveys conducted after the Lushan earthquake documented surface deformation features that are suggestive of slip on a fault to the west of the XF (Li et al., 2013; Xu et al., 2013). There is also a cluster of aftershocks that extends into the hanging wall (Fang et al., 2013; Fig. 2a), suggesting a southeast dipping fault in the hanging wall. 3D structural models based on seismic reflection profiles also indicate that there might be back reverse fault in the hanging wall (Li et al., 2014). To test whether the data require slip on a second southeast dipping fault, we included a fourth fault segment, F4, on the hanging-wall side of the main rupture (Fig. 2). For simplicity, we set the strike of F4 parallel with the main rupture and the same length, which is roughly consistent with the distribution of relocated aftershocks (Fang et al., 2013). We determine the dip of segment F4 by iterating over possible dips and inverting the geodetic data assuming uniform slip on segments F1–F4. We found that F4 is steeply dipping to the southeast at 60° (Fig. 2), and that the surface trace of F4 roughly corresponds to a mapped fault, which we refer to as the second branch of the SDF (Fig. 1b). We refer segment F4 as “the secondary fault” hereinafter.

Our final preferred fault geometry model is then composed of four planar fault segments. Segments F1–F3 approximating a listric fault associated with the main rupture of the Lushan earthquake, and segment F4 a steeply dipping, back reverse fault in the hanging wall (Fig. 2). We then use this fault geometry in our inversion of the spatiotemporal pattern of coseismic slip. Note that even though we assumed uniform slip on these segments in this initial analysis to determine fault dips, when we estimate the full coseismic slip no or negligible slip on any segment is permissible.

## 5. Inferred rupture model

Using the four-segment fault model determined from the geodetic data, we then jointly invert the local strong motion and geodetic data. The coseismic slip model obtained from the joint inversion is shown in Fig. 4. The minimum value of the assumed cost function is quite satisfactory (Fig. 3b and Fig. 5). The normalized root mean square error (NRMS) is 0.47, 0.2, and 0.5 for strong motion data, GPS and

InSAR measurements, respectively. The distribution of cumulative slip on the main fault is generally consistent with previously published models, and is dominated by thrust motion on segment F2 at the hypocentral depth (Hao et al., 2013; Zhang et al., 2014; Jiang et al., 2014). There is only minor slip on both the high-angle shallower fault segment F1 and the deeper detachment segment F3. There is a fairly significant amount of coseismic slip (~1 m of cumulative slip) inferred on segment F4 at depths shallower than the hypocentral depth, with the direction of slip pure dextral strike-slip to oblique reverse motion (Fig. 4d). Coseismic slip on segment F2 accounts for 45.6% of the total potency (computed as the sum of the slip times area in each of the subfaults) released in the Lushan earthquake, with slip on segments F1, F3, and F4 accounting for 15.3%, 15.5%, and 23.7% of the total potency, respectively. The seismic moment of our coseismic slip model is  $1.8 \times 10^{19}$  N m, equivalent to a moment magnitude of Mw6.8.

In Fig. 4, we show snapshots of the earthquake rupture process. Coseismic slip initiated on segment F2, and most of the thrust slip occurred during the first 5 s (Fig. 4a). During the next 5 s, the rupture propagated bilaterally on segment F2 to the northeast and southwest (Fig. 4b). Coincident with the bilateral propagation of slip, coseismic slip occurred on segment F4, and was largely dextral strike-slip. About 65% of the total potency was released in the first 10 s of the rupture. After that initial burst of coseismic slip, the rupture propagated to the shallower and deeper segments of the main fault, albeit with only minor amount of coseismic offsets (Fig. 4c). It should be noted that the inferred coseismic slip on segments F1 and F3 is largely inferred on isolated sub-faults, and it may be within the model noise. The total propagation ceased after 23 s.

### 5.1. Assessing the fault geometry

In contrast to the rather patchy inferred slip on segments F1 and F3, the inferred slip on segment F4 is less segmented and appears robust. However, we fully realize that there can be significant trade-offs between assumed fault geometry and inferred fault slip. To examine the robustness of the coseismic slip model, we inverted the data using fault models with a single planar fault and then with only the fault segments of the main fault (segments F1–F3).

Using a fault model composed of only one segment, with geometry similar to that used by Hao et al. (2013); Jiang et al. (2014), or Zhang

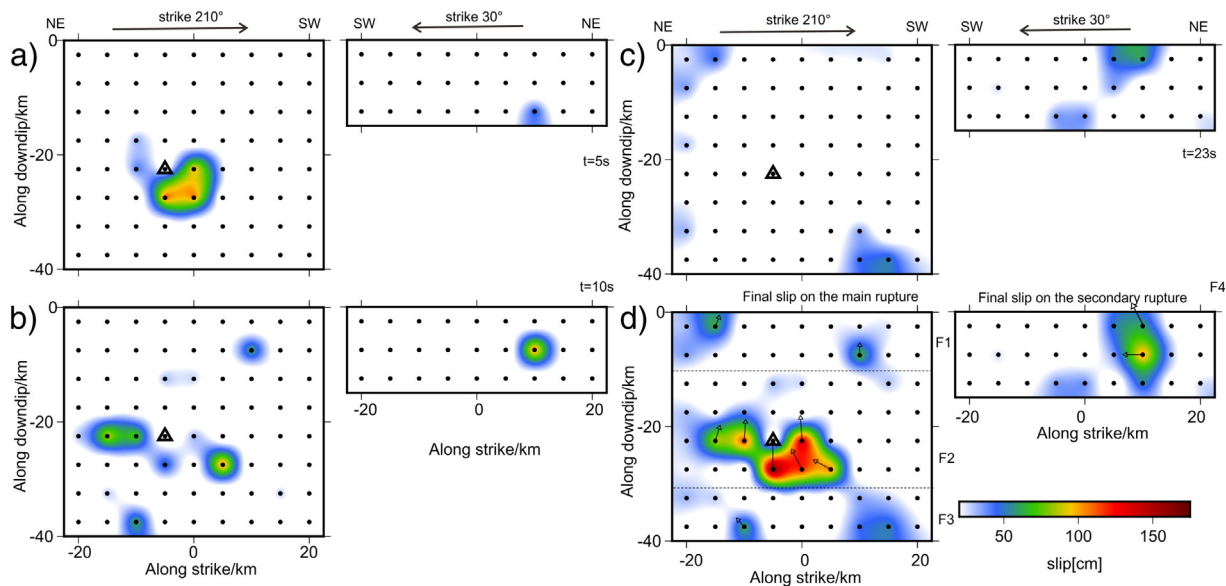


**Fig. 4.** Snapshots of the rupture process of the 2013 Lushan earthquake. Triangle is the hypocenter location. a) Snapshot of the rupture process during the first 5 s. b) Snapshot of the rupture process during 5–10 s. c) Snapshot of the rupture process during 10–23 s. d) The final static slip and rake distribution of the 2013 Lushan event (rake is shown only when slip is larger than 50 cm). For clarity, the 3 segments of the main fault have been jointed together.

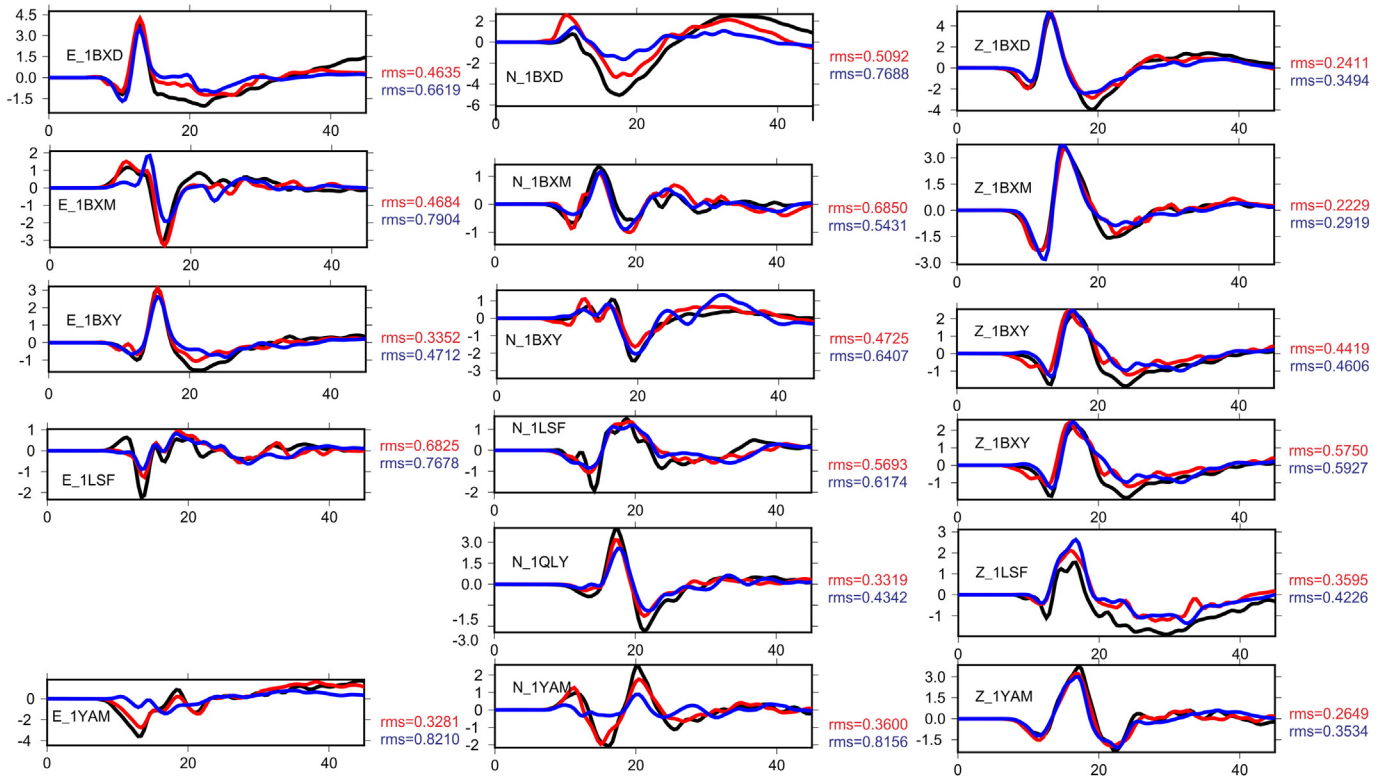


**Fig. 5.** Observed strong motion records at select near-field stations (black lines, see Fig. 1b for station locations), along with synthetic waveforms for the best fitting coseismic slip models determined without and with segment F4 (blue and red lines, respectively). The RMS values of each component from these two inversions are indicated, with text color corresponding to their waveforms. (For interpretation of the references to color in this figure legend, the reader is referred to the online version of this chapter.)

et al. (2014), we infer slip that is generally consistent with that found on segment F2 above, with mainly thrust slip constrained to depths of 10–20 km (see Supplementary material). However, the final fit to the strong motion data using a single planar fault is rather poor, especially compared to the strong motion data fits obtained in previously published coseismic slip models based on seismic data alone (Hao et al., 2013; Zhang et al., 2014). We note that our inversion differs from those, since we place an additional constraint that the cumulative fault slip also fits the geodetic data. This single fault segment model also has poor fit to the geodetic data, with NRMS of 0.4 and 0.55 for the GPS and InSAR data, respectively.

We then inverted the strong motion and geodetic data assuming only the main listric fault, composed of segments F1, F2, and F3 (see Supplementary material). The inferred slip distribution on these segments is similar, whether we include or do not include F4. Using only the main listric fault, model fit to the geodetic data is acceptable. The final fit to the strong motion data is acceptable for records from all stations except a few of the near field stations (Fig. 5). The most pronounced degradation of data fit by neglecting segment F4 is for station BXD, which is closest to the surface projection of segment F4. The improved fit to these strong motion stations is an indication that segment F4 slipped in the Lushan earthquake. While the inclusion of segment F4 does not dramatically improve the fit to the geodetic data, we find that when segment F4 is not included the inferred sense of slip is not consistent with the setting of the Lushan earthquake, which we discuss in Section 6.1.

## 6. Discussion

### 6.1. Consistency with prior models of strain accumulation

Tectonic and geodetic studies indicate that the Longmenshan fault system accommodates shortening and dextral deformation (e.g., Shen

et al., 2005; Burchfiel, 2008; Loveless and Meade, 2011). Block models using GPS data prior to the 2008 Wenchuan earthquake, find dip-slip and dextral strike-slip strain-accumulation rates of 1–2 mm/yr and ~1 mm/yr, respectively (Shen et al., 2005; Burchfiel, 2008), to as high as 3.2–4.2 mm/yr and 2.8–3.5 mm/yr, respectively (Loveless and Meade, 2011). As the sense of strain accumulation on the LMSF is reverse and dextral, one would expect that earthquakes on the LMSF would involve reverse and dextral slip. Indeed, the 2008 Wenchuan earthquake included both thrust and dextral strike-slip (e.g., Nakamura et al., 2010; Shen et al., 2009; Feng et al., 2010; Zhang et al., 2011; Wang et al., 2011). Previous coseismic slip models of the Lushan earthquake, based on the inversion of seismic data only, infer a component of dextral strike-slip (Hao et al., 2013; Zhang et al., 2014), as is also resolved in our preferred model (Fig. 4).

In contrast to the dextral sense of deformation on the LMSF, the coseismic slip model inferred from the GPS data, infers a sinistral component of strike-slip (Jiang et al., 2014). The inference of sinistral sense of strike slip was due to the coseismic jump to the southwest of the GPS sites in the hanging wall of the main reverse fault (Fig. 2). To explain the discrepancy in inferred sense of strike-slip, Jiang et al. (2014) argued that the block motion model may not be adequate to describe the crustal deformation field in the relatively complex region of the southern LMSF region where the Lushan earthquake occurred. In our preferred model, we infer dextral strike-slip on both the main and secondary faults, consistent with block models. The dextral strike-slip on the secondary fault largely explains the southwestward motion of the hanging wall GPS sites, while still allowing dextral strike-slip on the main fault. The fact that the inferred slip is more consistent with the inferred strain accumulation in this region (e.g., Shen et al., 2005; Burchfiel, 2008; Loveless and Meade, 2011) and the sense of slip in the Wenchuan earthquake (e.g., Nakamura et al., 2010; Shen et al., 2009; Feng et al., 2010; Zhang et al., 2011; Wang et al., 2011), together with the fact that the near-field strong motion records are better fit,

leads us to conclude that there was slip on the back reverse fault during the Lushan earthquake.

## 6.2. Aftershocks and Coulomb stress changes

The relocated aftershocks from Fang et al. (2013) are largely clustered in the hanging wall of the main listric thrust fault in our preferred fault model (Fig. 2a). Fang et al. (2013) also noted that most of the aftershocks were in the hanging wall, and that this is common for thrust earthquakes (e.g., Chang et al., 2000). Almost half of the aftershocks are between ~15 and ~22 km depths, the depth range in which the largest slip was located on the main thrust fault. Additionally, the cluster of aftershocks that extends into the hanging wall from the main thrust fault, begins roughly coincident with the largest slip we inferred. The aftershocks in the hanging wall cluster toward segment F4 in our preferred model. However, the density of aftershocks decreases at the depths in which our segment F4 starts.

Coulomb stress changes (CSC) due to cumulative coseismic slip quantify whether a given fault is pushed closer to, or further from, a given Navier–Coulomb failure criterion:

$$\text{CSC} = \tau - \mu \sigma,$$

where  $\tau$  and  $\sigma$  are shear and normal stress on a plane, respectively, and  $\mu$  is the effective coefficient of friction (King et al., 1994). King et al. (1994) found that there were more aftershocks following the 1992 Landers, CA earthquake in regions where CSC was larger than 0.1 MPa. We calculate CSC from the cumulative coseismic slip in our preferred model, assuming a coefficient of friction of 0.4 or 0.6. The static coefficient of friction of rock is often assumed to be 0.6 based on laboratory experiments (Byerlee, 1978), although pore fluid pressure can reduce the effective friction. Experiments on in-situ fault samples taken from a core of a portion of the fault that ruptured in the 2008 Wenchuan earthquake find coefficients of friction closer to 0.4 (Kuo et al., 2014). For simplicity, we calculate CSC on receiver faults with the same strike as the faults in our preferred model, and with dips ranging from 10° to 90°, both southeast and northwest dipping. Assuming that  $\mu = 0.4$ , we find that the CSC is larger than 0.1 MPa (0.5 MPa) at 97.5% (75.5%) of the relocated aftershock hypocenters (Fig. 6). Assuming that  $\mu = 0.6$ , these percentages drop slightly to 93.4% and 73.4% for aftershocks with CSC larger than 0.1 MPa or 0.5 MPa, respectively.

## 6.3. Back reverse fault slip

Our results indicate that there was likely coseismic slip on an opposing fault in the hanging-wall of the main thrust fault (segment F4; Fig. 2b). We find that this opposing fault is steeply dipping to the southeast, near conjugate to the main segment of the listric thrust fault that experienced the larger coseismic slip in the Lushan earthquake (segment F2). Without including this second fault, the local strong motion data, especially stations close to the epicenter, are less well fitted. Coseismic slip on the opposing fault included significant pure dextral strike slip or oblique thrust slip at shallower depth, indicating a back reverse fault (McClay and Buchanan, 1992).

Coseismic slip on segment F4 initiated about 5 s after coseismic slip initiated on the main thrust fault, after most of the coseismic thrust slip on segment F2 had occurred (Fig. 4). Slip on F4 initiated on the bottom of the segment, toward the NE edge of the fault. In contrast, we infer that slip on F2 during the first 5 s was slightly farther to the SW. We do not find that the data require any slip on a deeper extension of segment F4, closer to where it would intersect with segment F2. The CSC, due to the coseismic slip on the main fault segments in the first 5 s, on the F4 subfault in which rupture initiated is about 0.5 MPa (0.49 MPa, 0.53 MPa, and 0.56 MPa assuming a coefficient of friction of 0.6, 0.5, and 0.4, respectively). Based on this positive and significant CSC, as well as the rupture process, we envision that the Lushan earthquake initiated on a moderately-dipping segment of the SDF at depth and triggered slip on a back reverse fault represented by segment F4. Based on the coincidence of the surface projection of segment F4 and the trace of the SDF, we are interpreting the coseismic slip on segment F4 as buried slip in the SDF.

## 6.4. Inferred stress from coseismic slip

Using Bayesian estimation methods described in Medina Luna and Hetland (2013), we invert our coseismic slip model of the Lushan earthquake for the stress that led to that fault slip. The methodology is described in detail in Medina Luna and Hetland (2013) and Styron and Hetland (2015), and here we only briefly describe the methodology. Bayesian estimation results in a posterior distribution given a prior distribution and data constraints (see Mosegaard and Tarantola (1995) for a thorough discussion of Bayesian estimation methods). This inversion relies on the assumption that when the fault slips, it does so in the direction of the maximum shear stress resolved on the given fault surface, the so-called ‘Wallace–Bott’ assumption (Wallace, 1951; Bott, 1959),

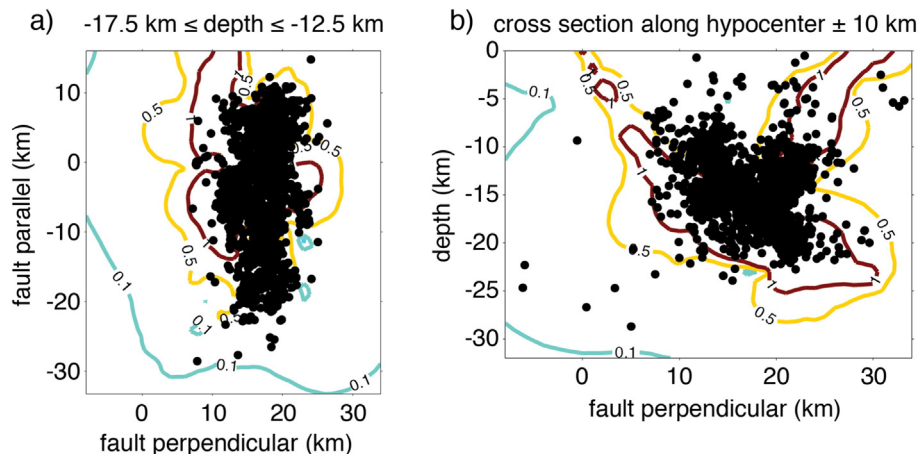


**Fig. 6.** Maximum CSC (contours), due to the cumulative slip in our preferred Lushan coseismic model (Fig. 4), between 12.5 and 17.5 km depths (a) and in a cross-section perpendicular to the trace of the faults and  $\pm 10$  km from the hypocenter location (b). Cyan, yellow, and red contours indicate CSC of 0.1 MPa, 0.5 MPa, and 1.0 MPa, respectively, and are labeled in units of MPa. Black dots are relocated aftershock from Fang et al. (2013) in the same volumes. (For interpretation of the references to color in this figure legend, the reader is referred to the online version of this chapter.)

which is assumed in all methods to infer stress from coseismic slip data (e.g., Michael, 1987; Reches, 1987; Angelier, 1994).

We follow a Bayesian Monte Carlo sampling strategy, in which samples of a prior stress are accepted in proportion to the likelihood of that stress being consistent with the coseismic slip model. In the following, “MCS”, “ICS”, and “LCS” refer to the most, intermediate, and least compressive stresses, respectively. We parameterize stress by the azimuth and plunge of the MCS, a rotation of the ICS and LCS directions about the MCS direction, the ratio of the magnitude of the LCS to MCS, and the magnitude of the ICS relative to the MCS and ICS. The absolute magnitude of stress is unconstrained from coseismic slip data (e.g., Célérier, 1988). For the prior, we assume that all stress orientations are equally likely, that all magnitudes of ICS are equally likely, and that the magnitude of the LCS is larger than 21% of the magnitude of the MCS. At LCS relative magnitudes less than this, an optimally oriented plane would fail under coefficients of friction of 0.85, equivalent to the low fault normal friction of Byerlee (1978). We assume that all LCS/MCS magnitude ratio are equally likely above 0.21, up to an isotropic state of stress. We compute the likelihood of each stress sample using a Gaussian likelihood function, where the direction of maximum shear stress on each fault segment is compared to the weighted average coseismic slip direction on that fault segment. We assume that the uncertainty of the coseismic slip direction is  $(s_i / S)15^\circ$ , where  $s_i$  is the maximum slip on each segment and  $S$  is the maximum slip on all segments. Weighting the error by slip magnitude is similar to as used by Medina Luna and Hetland (2013) and Styron and Hetland (2015), and has the effect as

to down weight low slip parts of the coseismic slip model that may be model noise.

Testing 500,000 prior samples, we find that our preferred coseismic slip model is consistent with an LCS plunging to the northwest, with steeper dips more likely (Fig. 7a). We find that MCS orientations are sub-horizontal, with the trend less resolved (Fig. 7a). ICS orientations are found to be dipping to the southwest (Fig. 7a). Note that a priori we assumed that isotropic stresses are as likely as those with large deviatoric components. A near isotropic stress may indeed predict that the direction of maximum shear stress on the fault segments corresponds to the coseismic slip rakes in our preferred Lushan slip model, although those shear stresses are much too low to be consistent with fault slip in a Coulomb frictional sense. We omit these near isotropic stresses by further constraining the inferred posterior stresses to include only stress models that are consistent with slip on the fault segments with a coefficient of static friction between 0.2 and 0.6. Constraining the posterior based on this mechanical criterion, we find that the most likely orientations of stress become even more likely, and that the less likely stresses prior to imposition of the mechanical constraint become even less likely. In sum, we find that the Lushan slip model is consistent with stresses characterized by sub-horizontal MCS orientations trending east–west to southeast–northwest, although more north–south trending MCS orientations are also possible, albeit lower likelihood (Fig. 7b). ICS orientations are shallowly dipping to the southwest, with dips around  $30^\circ$  most likely, and LCS is steeply dipping to the northeast (Fig. 7b). Furthermore, we find that the magnitude of LCS is

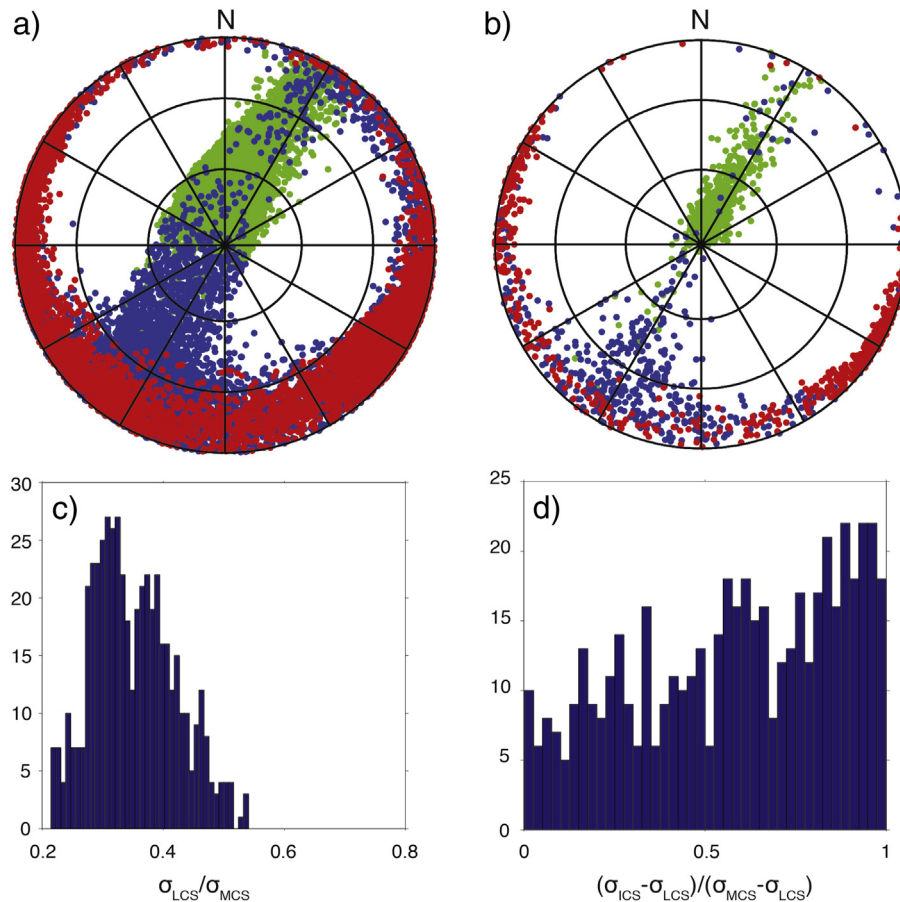


**Fig. 7.** (a) Orientations of principle stresses that are consistent with the Lushan coseismic slip. Dots are the lower hemisphere piercing points of the most (MCS; red), intermediate (ICS; blue), and least (LCS; green) compressive stresses in a Lambert equal area projection. Each radial line signifies  $30^\circ$  in trend and each circle indicated  $30^\circ$  in dip. (b) Orientations of principle stresses consistent with the Lushan slip model and Coulomb failure at frictions between 0.2 and 0.6 (colors as in (a)). (c) Relative magnitude of LCS compared to MCS magnitude for the stress models in (b). (d) Relative magnitude of ICS for the stress models in (b); 0 signifies  $\sigma_{ICS} = \sigma_{LCS}$  and 1 signifies  $\sigma_{ICS} = \sigma_{MCS}$ . (For interpretation of the references to color in this figure legend, the reader is referred to the online version of this chapter.)

around 30–40% of the magnitude of the MCS, and that the magnitude of the ICS is closer to the magnitude of the MCS than LSC (Fig. 7c–d).

Stresses inferred from our preferred Lushan coseismic slip model are not fully consistent with that inferred from multiple coseismic slip models of the Wenchuan earthquake, which are characterized by sub-horizontal MCS and ICS trending closer to east–west and north–south, respectively, and LCS steeply dipping to the northeast (Medina Luna and Hetland, 2013; Styron and Hetland, 2015). The stress inferred here does have some consistency with the stress inferred from thrust focal mechanisms of aftershocks following the 2008 Wenchuan earthquake along the LMSF range-front (Medina Luna and Hetland, 2013). It is important to note that the studies of Medina Luna and Hetland (2013) and Styron and Hetland (2015) both considered multiple coseismic slip models of the Wenchuan earthquake and that there was a much larger degree of complexity in both fault geometry and slip–rake in that earthquake. Hence, those results are likely more robust than inferences using one coseismic slip model of a much smaller earthquake. Nevertheless, these results indicated that the principal stress orientations in the Lushan earthquake regions might be rotated slightly to those in the northwestern region of the LMSF. The sense of the rotation is roughly clockwise, with MCS orientations rotated farther from the direction of the convergence of India and Tibet in the southwest of the LMSF.

## 7. Conclusion

We infer the rupture process of the 2013 Lushan earthquake using both seismic and geodetic data. We use a fault geometry model that is constrained by the geodetic data, which is a more complicated geometry than has been used previously. Our results show that two, roughly conjugate, faults may have ruptured during the 2013 Lushan earthquake. The largest moment release occurred on a northwest dipping, listric fault, predominantly as thrust slip, but with some dextral strike slip. A smaller burst of coseismic slip initiated on a steep, southeast dipping fault, with both thrust and dextral strike slip. This secondary coseismic slip initiated about 5 s after the Lushan earthquake began, and the coseismic potency was almost one quarter of the total potency in the Lushan earthquake. The coseismic slip is consistent with a sub-horizontal MCS orientation, trending east–west to southeast–northwest, a southwest dipping ICS orientation, and a steeply dipping LCS orientation, with LCS magnitude most likely about 30–40% of the MCS magnitude and the ICS magnitude closer to the MCS magnitude than the LCS. The sense of both thrust and dextral slip in the Lushan earthquake is roughly consistent with GPS based models of the sense of fault loading on the LMSF.

## Acknowledgments

This work is co-supported by grants of Chinese National Science Foundation (41461164002, 41474013, 41340008, 41374015) and funding from State Key Laboratory of Earthquake Dynamics, Institute of Geology, China Earthquake Administration (LED2014A01). Strong motion data is provided by the National Strong-Motion Observation Network System (NSMONS) of China. The topographic data is downloaded from: <http://srtm.csi.cgiar.org>. RadarSAT-2 SLC data is processed using the software Gamma. Figures are generated by Generic Mapping Tools (Wessel and Smith, 1998). We thank an anonymous review for a particularly thorough review.

## Appendix A. Supplementary data

Supplementary data to this article can be found online at <http://dx.doi.org/10.1016/j.tecto.2016.01.031>.

## References

- Angelier, J., 1994. Fault slip analysis and paleostress reconstruction. *Cont. Deformation* 4.
- Bott, M.H.P., 1959. The mechanics of oblique slip faulting. *Geol. Mag.* 96 (02), 109–117.
- Burchfiel, B.C., 2008. A geological and geophysical context for the Wenchuan earthquake of 12 May 2008, Sichuan, People's Republic of China. *GSA Today* 18 (7). <http://dx.doi.org/10.1130/GSATG18A.1>.
- Byerlee, J., 1978. Friction of rocks. *Pure Appl. Geophys.* 116 (4–5), 615–626.
- Célerier, B., 1988. How much does slip on a reactivated fault plane constrain the stress tensor? *Tectonics* 7 (6), 1257–1278.
- Chang, C., Wu, Y., Shin, T., Wang, C., 2000. Relocation of the 1999 Chi-Chi earthquake in Taiwan. *Terr. Atmos. Ocean. Sci.* 11 (3), 581–590.
- Delouis, B., Giardini, D., Lundgren, P., Salichon, J., 2002. Joint inversion of InSAR, GPS, teleseismic, and strong-motion data for the spatial and temporal distribution of earthquake slip: application to the 1999 Izmit mainshock. *Bull. Seismol. Soc. Am.* 92 (1), 278–299. <http://dx.doi.org/10.1785/0120000806>.
- Fang, L.H., Wu, J.P., Wang, W.L., et al., 2013. Relocation of mainshock and aftershock sequences of Ms7.0 Sichuan Lushan earthquake. *Chin Sci Bull* 58. <http://dx.doi.org/10.1007/s11434-013-6000-2>.
- Feng, G.C., Hetland, Eric A., X.L., Ding, Z.W., Li, Zhang, L., 2010. Coseismic fault slip of the 2008 Mw 7.9 Wenchuan earthquake estimated from InSAR and GPS measurements. *Geophys. Res. Lett.* 37, L01302. <http://dx.doi.org/10.1029/2009GL041213>.
- Gan, W.J., Zhang, P.Z., Shen, Z.K., et al., 2007. Present-day crustal motion within the Tibetan Plateau. *J. Geophys. Res.* 112, B08416. <http://dx.doi.org/10.1029/2005JB004120>.
- Hao, J., Ji, C., Wang, W., Yao, Z., 2013. Rupture history of the 2013 Mw 6.6 Lushan earthquake constrained with local strong motion and teleseismic body and surface waves. *Geophys. Res. Lett.* 40, 5371–5376. <http://dx.doi.org/10.1002/2013GL056876>.
- EM-DAT: The International Disaster Database, Centre for Research on the Epidemiology of Disaster, <http://www.emdat.be/>, accessed Apr 2015.
- Jiang, Z., et al., 2014. GPS constrained coseismic source and slip distribution of the 2013 Mw6.6 Lushan, China, earthquake and its tectonic implications. *Geophys. Res. Lett.* 41. <http://dx.doi.org/10.1002/2013GL058812>.
- Johnson, L., 1974. Green's function for Lamb's problem. *Geophys. J. R. Astron. Soc.* 37, 99–131.
- King, G.C.P., Stein, R.S., Lin, J., 1994. Static stress changes and the triggering of earthquakes. *Bull. Seismol. Soc. Am.* 84, 935–953.
- King, R., Shen, F., Burchfiel, B., Royden, L., Wang, E., Chen, Z., Liu, Y., Zhang, X., Zhao, J., Li, Y., 1997. Geodetic measurement of crustal motion in southwest china. *Geology* 25 (2), 179.
- Kuo, L.W., Li, H., Smith, S.A., Di Toro, G., Suppe, J., Song, S.R., ... Si, J., 2014. Gouge graphitization and dynamic fault weakening during the 2008 Mw 7.9 Wenchuan earthquake. *Geology* 42 (1), 47–50.
- Li, C., Xu, X., Gan, W., Wen, X., Zhang, W., Wei, Z., Xu, C., Tan, X., Chen, G., Liang, M., Li, X., 2013. Seismogenic structures associated with the 20 April 2013 Ms 7.0 Lushan earthquake, Sichuan province. *Seismol. Geol.* 35 (3), 671–683.
- Li, Y., Jia, D., Wang, M., Shaw, J., He, J., Lin, A., Xiong, L., Rao, G., 2014. Structural geometry of the source region for the 2013 Mw 6.6 Lushan earthquake: implication for earthquake hazard assessment along the Longmen Shan. *Earth Planet. Sci. Lett.* 390, 275–286.
- Liu, Q., Hilst, R., Li, Y., Yao, H., Chen, J., Guo, B., Qi, S., Wang, J., Huang, H., Li, S., 2014. Eastward expansion of the Tibetan Plateau by crustal flow and strain partitioning across faults. *Nat. Geosci.* 7 (5), 361–365.
- Loveless, J.P., Meade, B.J., 2011. Partitioning of localized and diffuse deformation in the Tibetan Plateau from joint inversions of geologic and geodetic observations. *Earth Planet. Sci. Lett.* 11–24.
- McClay, K.R., Buchanan, P.G., 1992. Thrust faults in inverted extensional basins. In: McClay, K.R. (Ed.), *Thrust Tectonics*. Springer, Netherlands, pp. 93–104.
- Meade, B.J., 2007. Present-day kinematics at the India–Asia collision zone. *Geology* 35, pp. 81–84.
- Medina Luna, L., Hetland, E.A., 2013. Regional stresses inferred from coseismic slip models of the 2008 Mw 7.9 Wenchuan, China, earthquake. *Tectonophysics* 584, 43–53.
- Michael, A.J., 1987. Use of focal mechanisms to determine stress: a control study. *J. Geophys. Res.* 92, 357–368.
- Mosegaard, K., Tarantola, A., 1995. Monte Carlo sampling of solutions to inverse problems. *J. Geophys. Res.* 100, 12431–12447.
- Nakamura, T., Tsuboi, S., Kaneda, Y., Yamanaka, Y., 2010. Rupture process of the 2008 Wenchuan, China earthquake inferred from teleseismic waveform inversion and forward modeling of broadband seismic waves. *Tectonophysics* 491 (s1–4), 72–84.
- Olson, A.H., Aspel, R.J., 1982. Finite fault and inverse theory with applications to the 1979 Imperial Valley earthquake. *Bull. Seismol. Soc. Am.* 72, 1969–2001.
- Parsons, T., Ji, C., Kirby, E., 2008. Stress changes from the 2008 Wenchuan earthquake and increased hazard in the Sichuan basin. *Nature* 454 (7203), 509–510.
- Reches, Z., 1987. Determination of the tectonic stress tensor from slip along faults that obey the coulomb yield condition. *Tectonics* 6 (6), 849–861.
- Savage, J.C., 1980. Dislocations in seismology. In: Navarro, F.R.N. (Ed.), *Dislocations in Solids*. North-Holland, Amsterdam.
- Shan, B., Xiong, X., Zheng, Y., Jin, B., Liu, C., Xie, Z., Xu, H., 2013. Stress changes on major faults caused by 2013 Lushan earthquake, and its relationship with 2008 Wenchuan earthquake. *Sci. China Earth Sci.* 2013. <http://dx.doi.org/10.1007/s11430-013-4642-1>.
- Shen, Z.-K., Lu, J., Wang, M., Burgmann, R., 2005. Contemporary crustal deformation around southeast borderland of Tibetan plateau. *J. Geophys. Res.* 110, B11409. <http://dx.doi.org/10.1029/2004JB003421>.
- Shen, Z.K., Sun, J.B., Zhang, P.Z., et al., 2009. Slip maxima at fault junctions and rupturing of barriers during the 2008 Wenchuan earthquake. *Nat. Geosci.* 2, 718–724. <http://dx.doi.org/10.1038/nego636>.
- Styron, R.H., Hetland, E.A., 2015. The weight of the mountains: constraints on tectonic stress, friction, and fluid pressure in the 2008 Wenchuan earthquake from estimates

- of topographic loading. *J. Geophys. Res. Solid Earth* 120. <http://dx.doi.org/10.1002/2014JB011338>.
- Thompson, B.T., Plesch, A., Shaw, J.H., Meade, B.J., 2015. Rapid slip-deficit rates at the eastern margin of the Tibetan Plateau prior to the 2008  $M_w$ 7.9 Wenchuan earthquake. *Geophys. Res. Lett.* 42.
- Wallace, R.E., 1951. Geometry of shearing stress and relation to faulting. *J. Geol.* 118–130.
- Wang, Y., Wang, E., Shen, Z., et al., 2008. GPS-constrained inversion of present-day slip rates along major faults of the Sichuan–Yunnan region, China. *Sci. China Earth Sci.* 51 (9), 1267–1283.
- Wang, Qi, Xuejun, Qiao, Qigui, Lan, Freymueller, Jeffrey, Yang, Shaomin, Xu, Caijun, Yang, Yonglin, Xinzhao, You, Tan, Kai, Gang, Chen, 2011. Rupture of deep faults in the 2008 Wenchuan earthquake and uplift of the Longmen Shan. *Nat. Geosci.* 4, 634–640. <http://dx.doi.org/10.1038/ngeo1210>.
- Wessel, P., Smith, W.H.F., 1998. New, improved version of Generic Mapping Tools released. *EOS Trans. Am. Geophys. Union* 79 (47), 579.
- Xu, X., Wen, X., Han, Z., et al., 2013. Lushan MS7.0 earthquake: a blind reserve-fault event. *Chin. Sci. Bull.* 58 (28–29), 3437–3443.
- Zhang, Pei-Zhen, 2013. Beware of slowly slipping faults. *Nat. Geosci.* 6, 323–324.
- Zhang, P.Z., Wen, X.Z., Shen, Z.K., et al., 2010. Oblique, high-angle, listric-reverse faulting and associated development of strain: the Wenchuan earthquake of May 12, 2008, Sichuan, China. *Annu. Rev. Earth Planet. Sci.* 38, 353–382. <http://dx.doi.org/10.1146/annurev-earth-040809-152602>.
- Zhang, G., Qu, C., Shan, X., et al., 2011. Slip distribution of the 2008 Wenchuan Ms 7.9 earthquake by joint inversion from GPS and InSAR measurements: a resolution test study. *Geophys. J. Int.* 186, 207–220. <http://dx.doi.org/10.1111/j.1365-246X.2011.05039.x>.
- Zhang, G., Vallée, M., Shan, X., Delouis, B., 2012. Evidence of sudden rupture of a large asperity during the 2008 Mw7.9 Wenchuan earthquake based on strong motion analysis. *Geophys. Res. Lett.* 39, L17303. <http://dx.doi.org/10.1029/2012GL052516>.
- Zhang, G., Shan, X., Delouis, B., Qu, C., Balestra, J., Li, Z., et al., 2013. Rupture history of the 2010 Ms 7.1 Yushu earthquake by joint inversion of teleseismic data and InSAR measurements. *Tectonophysics* 584 (1), 129–137.
- Zhang, Y., Wang, R., Chen, Y., Xu, L., Du, F., Jin, M., Tu, H., Dahm, T., 2014. Kinematic rupture model and hypocenter relocation of the 2013 Mw 6.6 Lushan earthquake constrained by strong-motion and teleseismic data. *Seismol. Res. Lett.* 85 (1). <http://dx.doi.org/10.1785/0220130126>.